PHILIPPINE ENGINEERING JOURNAL
PEJ 2022; Vol. 43, No. 1: 137-158

Received: 24 May 2022
Accepted: 15 June 2022

Structural Response Analysis of a Fiber-Reinforced Composite Horizontal Axis Tidal Turbine Blade using Blade Element Momentum-Derived Blade Loading

Jennifer F. Callanga, Louis Angelo M. Danao, and Binoe E. Abuan
Department of Mechanical Engineering, College of Engineering,
University of the Philippines Diliman
Quezon City, Philippines

Abstract — *The structural integrity of the newly designed rotor of a horizontal axis turbine blade was tested for structural response due to hydrodynamic loading. A verification and validation study using elliptical tube with isotropic material properties was conducted first to assess the accuracy of the numerical model. Further study involving the actual blade configuration with a spar was simulated using both orthotropic material properties of glass fiber reinforced polymer (GFRP) and carbon fiber reinforced polymer (CFRP) composites. A parametric study of ply angle and blade shell thickness was conducted to determine appropriate geometric configurations that will yield the lowest maximum principal stress and blade deformation. It was observed that the maximum principal stress is 154.44 MPa and the tip deflection is 139.66 mm for GFRP and 141.83 MPa with tip deflection of 68.26 mm for CFRP for shell thickness equivalent to 2% of the maximum blade chord length and a ply angle of 0°. When the ply angle is increased, the maximum principal stress increases with the worst condition at a ply angle of 45°. Shell thickness was studied, and results show that increasing the thickness decreased the maximum principal stress. When the shell thickness is increased to 8% of the maximum blade chord, the recorded maximum principal stress and tip deflection similarly decrease. It is determined that the present rotor blade is an improved design with good overall hydrodynamic performance and low stress and deformation levels.*

Keywords — Momentum, Composite, Finite Elements, Horizontal Axis, Tidal Turbine

I. INTRODUCTION

The present energy mix of the Philippines consists of about 40% renewable energy (RE) with geothermal energy comprising more than half of RE share [1]. This is an indication of a strong dependence to conventional forms of energy production based on fossil fuel. Despite this, the Philippines is still in a much better position versus first world countries when it comes to the penetration of RE in the energy production.

According to the Philippine Energy Plan of 2016-2030 [1], the potential resource contribution of offshore renewable energy (ORE) to the energy mix by 2030 will only be 71 MW despite the estimated 170 GW available potential [2]. With the available local expertise in ORE from resource assessment to device design and deployment, it is imperative that the untapped energy potential be exploited for the country’s benefit. The development of a device using local technology will ensure appropriate design and sustainable outcomes.

Tidal currents are highly predictable due to the well-documented behavior of the tides, and as such, it is an attractive source of renewable energy [3]. Tidal current systems use the kinetic energy available in water currents to turn turbines, similar to that of wind turbines. Recently, this method is becoming more favored because the implementation and maintenance cost is lower, and the environmental impact is lesser compared to tidal barrage systems [4]. These underwater machines resemble conventional modern machines in function with an obvious difference that they are entirely underwater. The blades are turned by water streams rather than wind which necessitates them to be shorter and stronger to withstand higher hydrodynamic forces.

Several types of tidal current machines are available. One of the more popular is the horizontal axis tidal turbine (HATT). It is an axial flow machine and is very close in concept to large scale wind turbine installations. It has received much research and development over other types resulting in the most number of developers and manufacturers worldwide. A survey of the tidal current machine developers at present reveals that about 50% produce axial flow devices [5]. It can only be surmised that this is a convenient offshoot from the very mature technologies established in the axial flow wind turbine concept that are directly translatable into axial flow water turbines.

This research utilized a two-fold approach in the analysis of the horizontal tidal turbine blade (HATT) design. A hydrodynamics performance study based on Blade Element Momentum Theory (BEMT) was conducted first to provide the blade specifications such as the chord length, twist angle, and foil profile. Using the same approach, the individual blade loading and other forces acting on the blade associated with the fluid flow were determined. The static structural analysis follows the hydrodynamic performance study to validate the integrity of the blade for the intended use. Due to the density of seawater, it is expected that the loads on the blades are significantly high. Thus, it is important that the blade is structurally sound when operating under extreme conditions. However, actual testing and experiments of this blade is expensive and risk extensive. That is why numerical methods are developed to study turbine designs. Moreover, the limited availability of structural performance data from the literature on tidal turbine blades has driven the authors to follow a twofold approach for the structural analysis.

This paper focused only on the static structural analysis of a tidal turbine composite blade. This study aims to investigate the structural response of a fiber-reinforced composite proposed blade under different loading conditions to identify the critical zone on the blade and determine the possibility of blade failure. A parametric study on ply angle, blade materials, and shell thickness follow using the Ansys Mechanical module and Ansys Composite Module.

II. MATERIALS AND METHODS

2.1 Proposed Blade Characteristics

The turbine geometry used in this paper was the result of the hydrodynamics performance study in the companion research [6]. It was created with the aid of QBlade [7], an open source software that is capable of designing custom blade geometry and calculating the performance polars of different airfoil profiles. The blade profiles can either be generated through XFOIL/XFLR5 functionality of the software or it can be imported from the designer's custom designs.

The proposed blade is not designed from scratch. Its profile was based on the tidal turbine used by Batten et al. [8] and Bahaj et al. [9] in their experimental investigations on HATT. The NACA 44xx foil series was used as cross-section for the blades instead of the 63-8xx series in the Batten blade. The NACA 44xx series was selected because of its good lift performance and good lift to drag ratio even at post stall angle of attack [10]. Additionally, using this foil profile resulted in a better performance curve of the proposed blade compared to that of Batten. This is shown in Figure 1, where the performance curve of the two blades in terms of the power coefficient (C_p) and tip speed ratio (TSR) were plotted. It can be observed that the C_p vs TSR curve of the proposed blade is wider in contrast to the steeper curve of Batten. Also, the power coefficient of the proposed blade is relatively high for a wider range of TSRs which implies that for a broader range of flow conditions, it can still operate with good performance.

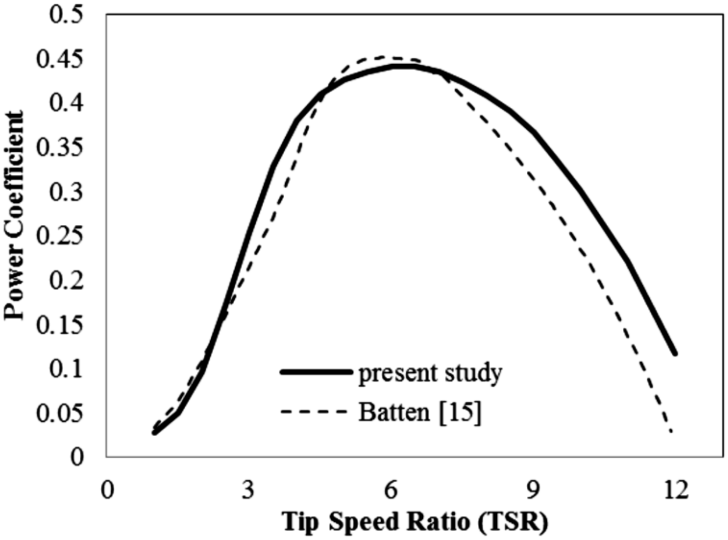

Figure 1. Performance curve of the two blades being studied [6].

After the performance curve of has been determined, the 3D shell model of the proposed blade based on the optimized blade geometry specifications from Qblade was developed in Ansys Spaceclaim, a modeling CAD component of the Ansys software. Each coordinate of the NACA44xx foil profile was imported into Spaceclaim to create the 2D sketch of the blade. The loft/skin feature of the software was then used to build the surface between each profile. The generated blade profile has a thickness of 5 mm and a length of 1.8 m. A 20 mm spar was added to improve the stiffness of the blade. Figure 2 shows the image of the 3D shell model of 44xx-based blade, and the new tidal turbine rotor.

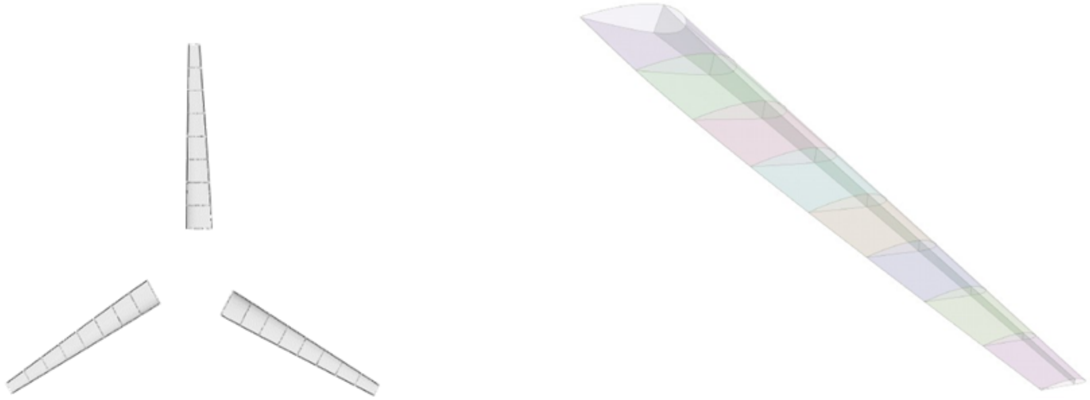

Figure 2. Proposed HATT CAD model: a) rotor b) 3D shell [6].

2.2 Boundary Conditions

The input loads applied to the proposed blade were the hydrodynamic forces generated from the BEM Solver of the QBlade software. The normal and tangential loads were assigned, following the BEM results, at each station on the blade. Both forces were applied as "Remote Force" type and over the entire section surface to avoid local stress concentrations as shown in Figure 3. A rotational velocity was also added on the rotor for completeness of the solution. Additionally, the root of the blade was constrained to move in the X, Y, and Z directions as it was assigned as fixed support creating a cantilevered beam.

To investigate a more practical rotor size, the proposed rotor was scaled five times its original size to 2 meters blade length (the average size of small-size HATT). From the simulations, the power computed at a velocity of 2 m/s reaches a value of 20 kW.

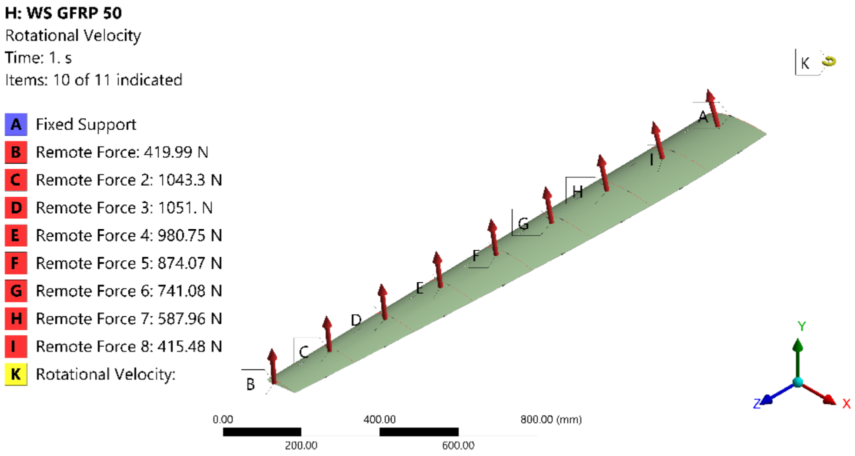

Figure 3. Pertinent boundary conditions as applied to the blade geometry.

2.3 Material Selection

Finding the suitable material for the tidal turbine blade is one of the most important considerations that affect the efficiency and longevity of the turbine [11]. Tidal turbine blades are continuously exposed to extreme conditions, i.e., nonuniform and varying hydrodynamic loads from tidal currents, and corrosion due to high chemicals in seawater, which can consequently degrade the quality of the blade material [12]. Thus, it is important that the material to be used can withstand corrosion while maintaining its strength and stiffness. Fiber-reinforced polymer composite (FRP), having excellent mechanical properties, is an appropriate choice. FRP composites are widely used materials in the field of renewable energy and has established its reputation in the wind industry [13]. However, due to the difference in the chemical composition of air and seawater environment, several studies were conducted to test the suitability of FRP in marine setting. Structural integrity and durability of composite materials when continuously exposed to salt water were investigated and it was found out that the mechanical properties and performance of composite structures are greatly affected by moisture, temperature, ultraviolet radiation, and pH level of water [14]–[16]. To address these issues, extensive research were done to enhance the strength of composites by changing its material composition, geometrical form, fiber-matrix relationship, fiber orientation, etc. [17]–[19]. Despite these shortcomings and given the advancement in FRP composites, it is with no doubt that it is still the best alternative to the conventional homogeneous materials in marine applications [14], [16], [20], [21].

In this study, two multi-layered cross woven FRP composite materials were used. Carbon fiber-reinforced polymer (CFRP) and glass fiber-reinforced polymer (GFRP), both infused in the epoxy resin matrix, were utilized as the blade materials. These two composites were modeled as orthotropic. Table 1 shows Young's modulus, Poisson's ratio, and density of the different blade materials.

Table 1. Mechanical property values of different blade materials [22].

Material	Young's Modulus, MPa	Poisson's Ratio	Density, g/cm^3	Ultimate Strength, MPa
Carbon fiber-reinforced composite (CFRC)	91,820 (X direction)	0.05 (XY)	1.48	4,000
	91,820 (Y direction)	0.3 (YZ)		
	9,000 (Z direction)	0.3 (XZ)		
Glass fiber reinforced composite (GFRC)	45,000 (X direction)	0.3 (XY)	2.00	1,229
	45,000 (Y direction)	0.4 (YZ)		
	10,000 (Z direction)	0.3 (XZ)		

2.4 Composite Characterization

Composites are highly orthotropic materials where fiber orientation significantly influences its mechanical properties. The strength of the composite is greatest along the longitudinal direction of fibers [23]. Based on the study conducted by Walczyk [24], the recommended ply arrangement for glass epoxy layers for a wind turbine is [45°/90°/0°/-45°/-45°/0°/90°/45°] as shown in Figure 4a. The Ansys ACP PrepPost module was used to characterize the direction of the fibers for the current study. This is a built-in module in the

Ansys software that allows the assignment of composite material, fiber orientation, laminate stack up, and the fabric thickness. Upon uploading the 3D shell model of the blade to Ansys ACP, the blade profile was divided into an upper and lower surface each divided further into nine sectors. This was done to define the reference fiber direction easily. The FRP layers for the proposed blade were arranged such that the spanwise direction is along the fiber direction (0 – 180° line). This was considered the baseline ply angle setting that was subjected to a parametric study. Each ply layer in this configuration was set to have the same thickness. Figure 4b shows the ply angle oriented in the 0°-180° direction.

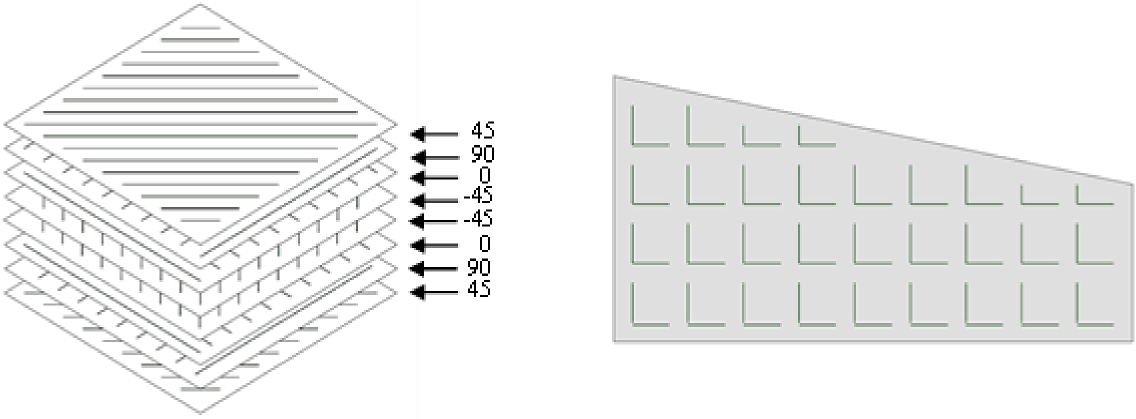

Figure 4. Ply orientation a) as suggested by Walczyk, b) for the current study.

2.5 Mesh Generation and Mesh Density Analysis

The surface model of the proposed blade was imported into ANSYS mechanical module for mesh generation and FEA modelling. The mapped face meshing control in the software was used to ensure that the mesh is mainly composed of quad elements as shown in Figure 5. The blade geometry was meshed using SHELL181, a 4-node structural shell element used to analyze layered geometries [25]. The quality of the mesh was evaluated for possible element distortion or irregularities using the different mesh metric checks available in ANSYS Mechanical. For this model, the warpage of quad elements was inspected. Warpage is the amount of deviation of an element from a flat one. Typical values of the warping factor are from 0 to 1 [26]. In the current study, a warping factor of 0.004 was obtained and is generally acceptable.

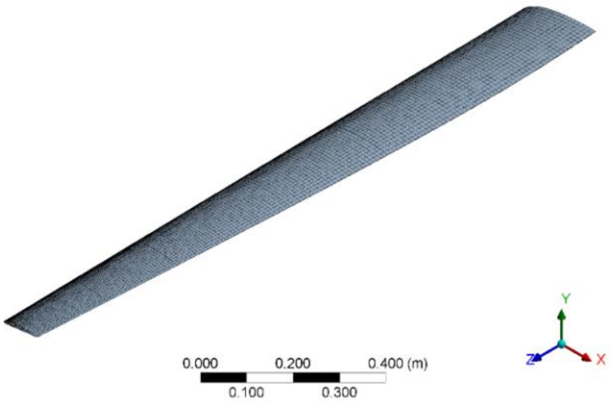

Figure 5. Meshing parameters applied to the blade.

To confirm the convergence of the results, a mesh density study was conducted. This is to ensure efficient usage of the storage capacity without compromising accuracy. In this study, the mesh was refined by adjusting the element size and the capture curvature minimum size. From Table 2, at the coarsest mesh level, shown as mesh A, the maximum principal stress is 154.69 MPa and a deformation of 139.83 mm. Decreasing the element size from 100 mm to 25 mm doubles the number of elements from 19,180 to 40,454. However, despite this increase, there is no significant change in the maximum principal stress and deformation values. Given the results, mesh B was determined to be sufficient to be used for the remaining simulation.

Table 2. Results of mesh refinement on the turbine blade.

	number of elements	**maximum principal stress**	**directional deformation**
mesh A	19180	154.69 MPa	139.85 mm
mesh B	30644	154.85 MPa	139.59 mm
mesh C	40454	154.85 MPa	139.41 mm

III. STRUCTURAL RESPONSE STUDY

Static structural analysis was done to assess the structural response of the proposed blade subjected to various loading conditions using a parametric analysis that deals with the effect of hydrodynamic loads, type of composite, blade dimension, and ply orientation. The structural response of the blade in terms of stress and deformation distribution was analyzed to identify the critical zone and determine the possibility of blade failure. The optimized blade geometry and blade load distribution from the hydrodynamics study were used as the boundary conditions for the analysis. The numerical model was validated against analytical solution using an elliptical tube with gross dimensions similar to the blade. Afterwards, the verified method is used in the analysis of the actual blade.

3.1 Validation and Verification Study

A numerical verification was undertaken to examine the accuracy of the FEA model. An elliptical tube was modeled to represent the simplified geometry of the proposed blade. The ellipse has a minor diameter of 62.5 mm and a major diameter of 250 mm. These values are proportional to the dimensions of the actual blade profile. The tube has length of 1.8 m similar to the length of the proposed blade and the shell thickness is set to 5 mm. The boundary conditions intended to be applied to the actual blade was used as the input parameters in the verification study. As discussed in the previous section, the blade root portion was assigned as fixed support to create a cantilevered beam. Figure 6 shows the 500 N/m load applied to the length of the blade. This load is comparable to the expected range of loading of the actual blade. The loading is approximated by multiple point loads instead of a line load because blade loading data from the BEM study are similarly piecewise. The elliptical tube was meshed using the same settings as the mesh B in the mesh density study.

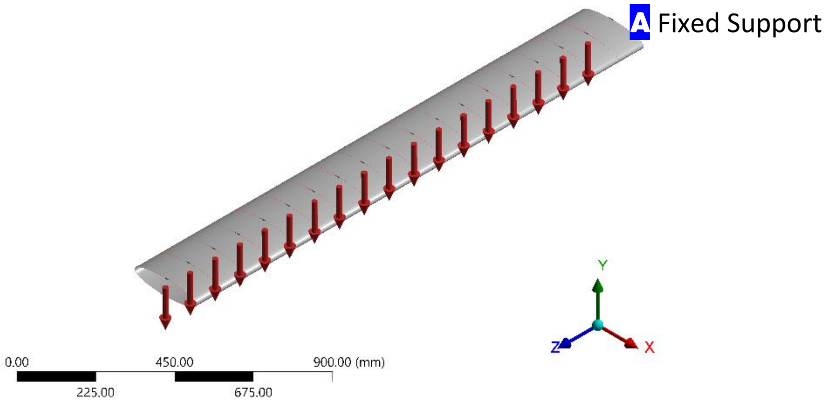

Figure 6. Boundary conditions applied to the elliptical tube

Table 3 shows the mechanical properties of the fiberglass composite used in the analysis. The material was assumed to be homogeneous, isotropic, and linearly elastic for simplification.

Table 3. Material properties of fiberglass composite [27].

Material	**Young's Modulus, E (MPa)**	**Density, ρ (g/cm^3)**	**Poisson's ratio, ν**
Fiberglass composite	20,000	1.85	0.3

Analytical computation was carried out using equations and assumptions presented in Shigley's Mechanical Engineering Design book [28]. Figure 7 shows the schematic diagram of the cantilevered beam with the applicable forces and restrictions. The beam is assumed to be straight and have a constant cross section and is symmetric along the plane of bending. Also, it is assumed to be subjected to pure bending load only and as such, the effect of shear forces is zero. Given these conditions, the maximum bending stress for a cantilevered beam is expected to be located at the support.

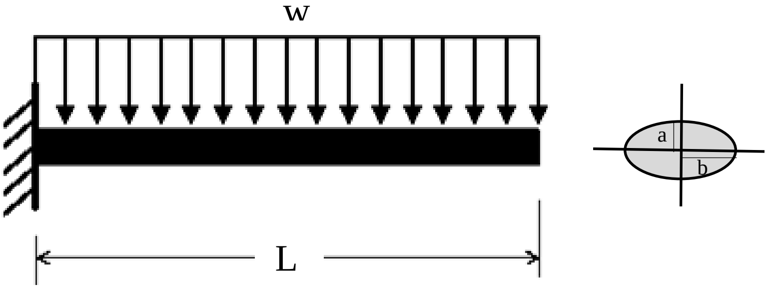

Figure 7. Schematic diagram of boundary conditions on cantilevered beam [27].

The magnitude of the bending stress, σ, is computed using equation 1.

$$\sigma_{bending} = \frac{My}{I} \quad \text{Eq. 1}$$

where
σ – bending stress
M – bending moment
I – second area moment

The second area moment for a cantilevered beam with an elliptical cross section is given by equation 2.

$$I_x = \frac{\pi}{4} ab^3 \quad \text{Eq. 2}$$

where a and b are the minor and major diameters, respectively.

$$\delta_{max} = \frac{wL^4}{8EI} \quad \text{Eq. 3}$$

The maximum deflection, **δ**, on the beam was computed using equation Eq. 3, where the ***w*** is the load applied uniformly along the length **L** of the beam divided by the Young's modulus **E** of the fiberglass and the second moment of inertia, **I**.

The total strain energy, ***U***, due to bending of a cantilever beam under uniformly distributed load can be determined by

$$U = \int_0^L \frac{M^2}{2EI} dx \quad \text{Eq. 4}$$

Computation for the analytical values is shown below. Given the second area moment to be 1.291E-6 m^4 and bending moment to be 810 N-m, the bending stress was computed to be

19.6 MPa and the maximum tip deflection to be 25.404 mm. Strain energy of the beam was also obtained using equation [4] and the result was 4.57 Joules.

$$\sigma_{bending} = \frac{810(0.03125)}{1.291\ x\ 10^{-6}} = 19.6021\ MPa$$

$$\delta_{max} = \frac{500(1.8)^4}{8(2x10^{10})(1.291x10^{-6})} = 25.404\ mm$$

The results of the verification study are presented in Table 4. It can be observed that the Von mises stress from the numerical simulation is higher than the analytical values. On the other hand, the deformation value from the simulation is lower compared to the analytical computation. This slight difference can be attributed to several factors. First, numerical simulation assumed piecewise load application, whereas a uniformly distributed load was used in the analytical computation. The computation of second moment of inertia could also be another factor. In the analytical computation, it was approximated by subtracting the moment of inertia of the smaller ellipse from the moment of inertia of the bigger ellipse. Also, in the analytical calculation, the beam was assumed to follow the linear, small displacement theory, while the numerical simulation considers the non-linear effects in the analysis.

Table 4. Verification results for the elliptical model.

	Von Mises stress	Directional deformation	Total Strain Energy
numerical simulation	22.201 MPa	25.049 mm	4.57 J
analytical calculation	19.601 MPa	25.404 mm	4.61 J

Closer scrutiny of the results in Figure 8a reveals that for both models, the highest Von mises stress value can be found at the fixed end as expected for the cantilevered beam. However, for the numerical simulation, the free end reveals a stress value of 40.93 kPa at the minor radius location of the section. From an analytical perspective, there should be no stress at this location since the bending moment should be zero. However, the distributed load still induces shear effects on the beam resulting in a non–zero Von Mises stress value computed at this point.

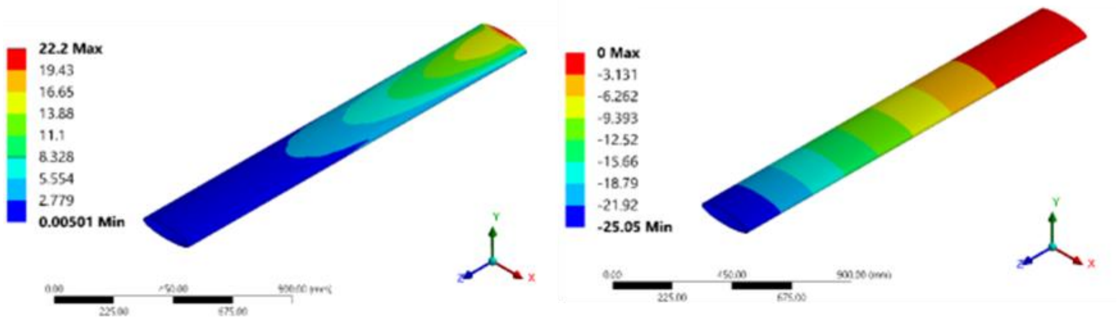

(a) (b)

Figure 8. Simulation results showing (a) Von Mises stress and (b) directional deformation.

Further analysis was conducted by adding a 20 mm web along the length of the elliptical tube to mimic the spar on the actual blade. The model was simulated, and the results were compared against analytical computation. Similar assumptions were made regarding the analytical solution. The FEA model is meshed using the same settings as the previous case. The main difference in this model is the presence of a spanwise web that adds bending stiffness along the loading plane. As with the results in the previous analysis, there is a slight difference in the listed values as seen in Table 5. The maximum Von mises stress from the simulation was 15.451 MPa while the analytical computation resulted in 14.905 MPa. The location of the maximum stresses for both models are still in the fixed end of the beam as shown in Figure 9. The maximum deflection obtained from the simulation was 18.713 mm, 3 % lower than the computed deformation. Nevertheless, the results of the analysis for both cases are in good correlation and can be considered acceptable. This establishes the numerical method as a reliable tool for the structural analysis of an actual tidal current blade.

Table 5. Verification results for the tube with web model.

	Von Mises stress	**Directional deformation**
FEA	15.451 MPa	18.713 mm
analytical	14.905 MPa	19.317 mm

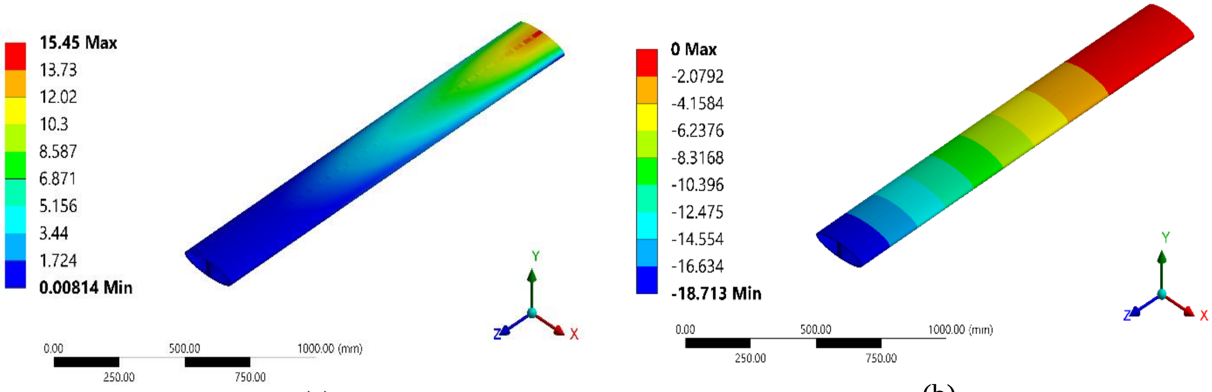

(a) (b)

Figure 9. Simulation results showing (a) Von Mises stress and (b) directional deformation for tube with web.

3.2 Numerical Analysis of Tidal Turbine Blade

Upon verifying the capability of ANSY software and the accuracy of the numerical model, the established methodology was utilized in the analysis of the optimized proposed blade design. Input parameters discussed in the preceding sections were implemented using the same approach to the validation study.

3.2.1 Composite Material

To simulate the actual properties and characteristics of the blade, the analysis is transferred to the Ansys Composite PrepPost Module where composite-related input parameters are set up. The two FRP materials used in the simulation are CFRP and GFRP. However, since only a unidirectional GFRP is available in the Ansys material database, its mechanical properties were altered to mimic a woven, orthotropic composite as shown Table 1. A plot of the polar properties of the elastic modulus for CFRP and GFRP is shown in Figure 10. As seen in the figure, the maximum elastic modulus value of 91.830 GPa for CFRP and 45 GPa for GFRP is along perpendicular directions that follow the fiber orientation.

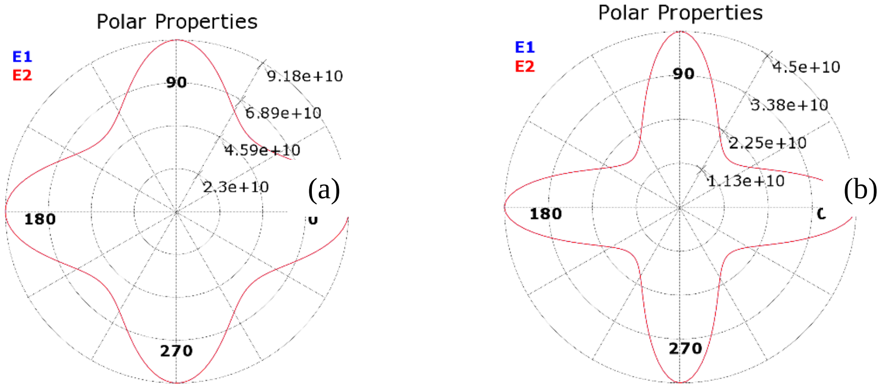

Figure 10. Orthotropic elastic modulus of a) woven carbon fiber reinforced epoxy, b) EGlass reinforced Epoxy.

For the orthotropic analysis, the critical parameter monitored is the maximum principal stress and the directional deformation along y-axis. From Figure 11a and 12a, it can be observed that the maximum principal stress is located at approximately one third from the blade root. A likely reason for the results is that this portion of the blade has a rapid change in blade thickness. From the root, the hydrofoil thicknesses are 24%, 20%, and 18% at 0.2 m intervals. From here on, a more gradual change in foil thickness is used at 1% change every succeeding station. The maximum y-deflection, shown in Figure 11b, is observed to be the tip of the blade at 139.9 mm. This value is equivalent to 7.8% of the blade length. Similar trends are observed with the CFRP blade. The recorded maximum principal stress is 141.83 MPa, 10% lower than GFRP. Figure 11b and 12b shows that CFRP blade is less likely to deform compared to GFRP blade with the former having a maximum tip deflection of only 68.26 mm. The maximum principal stress is observed on the same region as that of the GFRP.

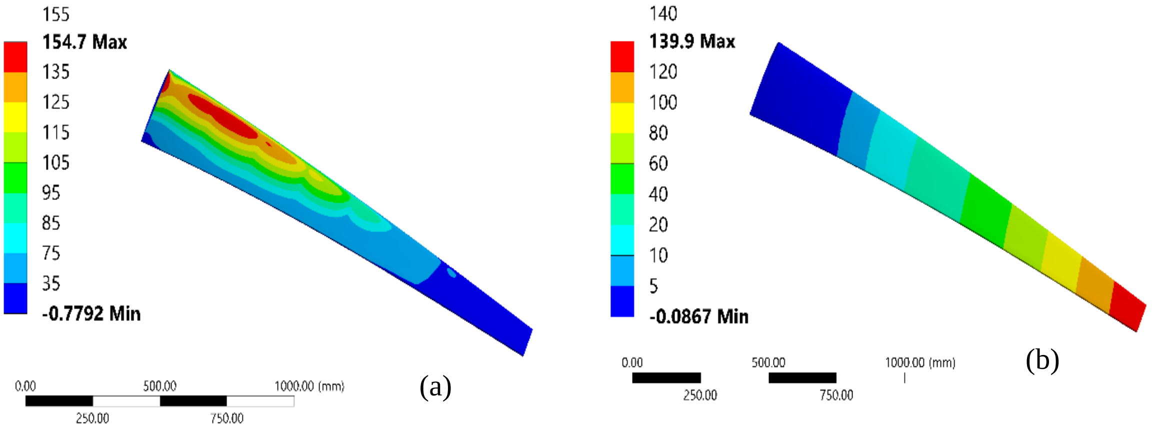

(a) (b)

Figure 11. Orthrotropic analysis results for GFRP:
(a) maximum principal stress, (b) directional deformation.

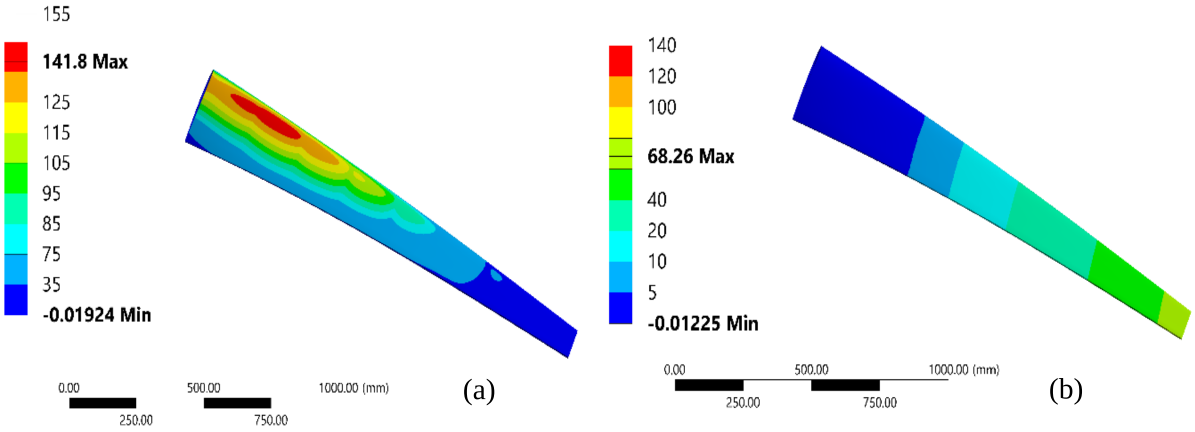

(a) (b)

Figure 12. Orthotropic analysis results for CFRP:
(a) maximum principal stress, (b) directional deformation.

3.2.2 Ply Angle

The blade ply angle was studied in order to ascertain the most appropriate orientation of the fabric in relation to the blade span direction. The simulations were carried out using three additional ply angles: 30°, 45°, and 60° anti-clockwise (Figure 14b, c, and d, respectively). The baseline case is 0° (Figure 14a) and is the orientation used for the simulation of the previous section (Orthotropic Analysis).

Table 6 shows the results for the ply angle study. The best case is the ply orientation where one fiber direction is along the blade span direction (0°) with the lowest stress value of 154.44 MPa for GFRP and 141.81 for CFRP. All other cases produced higher stress values of maximum principal stress but still way less than the ultimate strength of the materials. The worst case is ply angle of 45° where the maximum principal stress is recorded at 335.55 MPa for GFRP and 204.84 MPa for CFRP, an almost 50% increase in stress value. It can also be observed that the maximum nodal deflection is lowest for the baseline case with a value of 139.66 mm and 68.26 mm for GFRP and CFRP respectively. The worst case is still the 45° ply angle with a tip deflection of more than twice the baseline results at 368.00 mm and 112.3 mm. As can be observed in Figure 13, the tip deflection of GFRP blade at the worst ply angle accounts for about 20% of the blade span length. Whereas for the CFRP blade, the tip deflection at 45° angle is only about 6% of the total length. From this study, it can be said that the most appropriate ply angle is 0° as this provides the greatest strength and lowest stress level. This observation agrees with the presented mechanical properties of the composite materials in Table 1 and the polar plot in Figure 10 where the modulus of elasticity is maximum along the longitudinal (0°) and transverse (90°) directions and least along 45° orientation. Also, the degree of deformation of GFRP is greater compared to CFRP due to a higher value of Young's modulus of the latter.

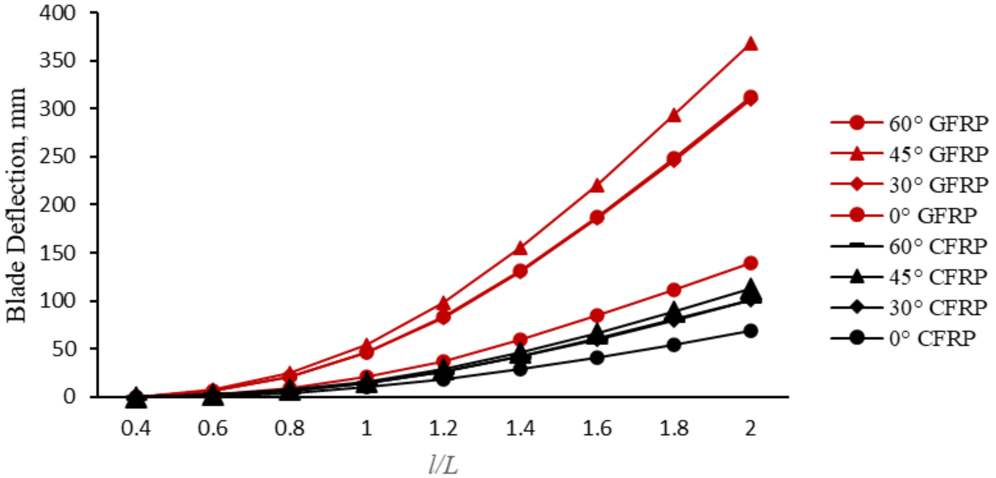

Figure 13. Deflection along blade span for different ply angle orientations.

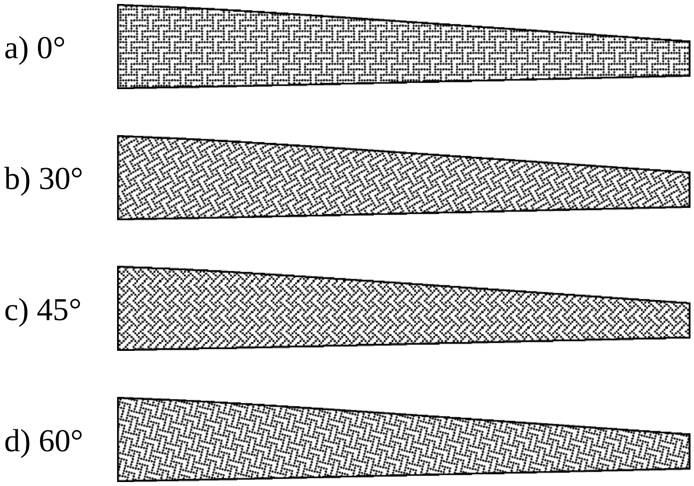

Figure 14. Orientation of ply weave angle relative to blade span.

Table 6. Results of ply angle study for GFRP and CFRP.

ply angle (deg)	GFRP	CFRP
	maximum principal stress (MPa)	maximum principal stress (MPa)
0	154.44	141.83
30	279.71	182.54
45	335.55	204.84
60	316.69	200.32

3.2.3 Shell Thickness

To investigate the effect of blade shell thickness on the stress levels and blade deformation, a thickness study was conducted using three thickness levels. The baseline thickness used was still the original blade thickness of the Orthotropic Analysis section at 5 mm (2%). Two additional thicknesses were studied based on the specific percentage of the maximum blade chord: 12.5 mm (5%), and 20 mm (8%). Additionally, two flow conditions were studied to investigate the stress and deformation on the blade at an average flow velocity of 2 m/s and extreme flow velocity of 5 m/s.

Table 7 shows the results of the thickness study with the two flow conditions. As the wall thickness increases, the levels of maximum principal stress and directional deformation decreases. This pattern is true for both flow conditions and for both materials. At a wall thickness of 20 mm, the maximum principal stress is 32.6 MPa for GFRP and 29.6 MPa for CFRP for the 2 m/s flow, while the recorded maximum stresses at 5 m/s flow are 77.8 MPa and 69.8MPa for GFRP and CFRP respectively. These values are significantly lower than the observed stresses at 5 mm thickness. The deformation response of the model on varying layer thicknesses shows the same trend with that of the maximum principal stress. From the baseline total deformation of 139.66 mm for GFRP, the value decreases to 16.24 mm for higher thicknesses. It is also noted that the deformation values of CFRP are significantly lower compared to GFRP due to its higher stiffness. It was observed that for both materials, the thickness of the blade is inversely proportional to the maximum principal stress and to the amount of deformation exhibited by the model owing to its higher cross-sectional resistance.

On the other hand, an investigation on the effect of flow velocity to the maximum principal stress and tip deflection was also carried out. At 2 m/s flow, the recorded maximum principal stress in GFRP was 154.44 MPa and 141.83 for CFRP. Increasing the flow velocity to 5m/s also increases the maximum principal stress levels doubling up the baseline values. A similar trend is observed for the tip deflection where values of the nodal displacements more than double when the flow conditions change from 2 m/s to 5 m/s. From the baseline deflection of 139.7 mm for GFRP, the value increases to 317.04 mm for the thinnest blade. The thickest blade also shows significant deflection at 5 m/s flow with an increase to 38.13 mm from the 2 m/s results of 16.24 mm. The same observation can be said for CFRP blade. These findings are as expected, since increasing the flow velocity induces an increase in the hydrodynamics loading on the blade.

Table 7. Results of the shell thickness study for GFRP and CFRP.

shell thickness (mm)	GFRP				CFRP			
	maximum principal stress (MPa)		directional deformation (mm)		maximum principal stress (MPa)		directional deformation (mm)	
	2 m/s	*5 m/s*	*2 m/s*	*5 m/s*	*2 m/s*	*5 m/s*	*2 m/s*	*5 m/s*
5	154.44	355.61	139.66	317.04	141.83	322.34	68.26	2.369
12.5	58.397	138.23	39.29	86.47	54.489	121.03	19.18	6.514
20	32.599	77.813	16.24	38.13	29.581	69.832	7.929	12.02

IV. FAILURE ANALYSIS OF COMPOSITE

One of the main factors to consider in analyzing composite material is the forces experienced by each lamina. There are several failure criteria developed to determine the failure of FRP composites. Two of the most common criteria used to predict first-ply failure are Tsai-Hill and Tsai-Wu failure criteria [29]. For this study, Tsai-Wu criteria was employed. This was developed by Stephen Tsai and Edward Wu of the US Air Force Materials Laboratory in order to get a better fit with the test data [30]. This is an interactive criterion wherein it uses a second order polynomial equation that involves all stress or strain components to determine the failure load. This can be applied for both 2D and 3D state of stress [31]. The criterion predicts that failure occurs when

$$F_i\sigma_i + F_{ij}\sigma_i\sigma_j \geq 1 \qquad \text{Eq. 5}$$

For plane stress applications, the Tsai-Wu criterion is reduced to the form

$$F_{11}\sigma_{11} + F_2\sigma_{22} + F_{11}{\sigma_{11}}^2 + F_{22}{\sigma_{22}}^2 + 2F_{12}\sigma_{11}\sigma_{22} + F_{66}{\tau_{12}}^2 = 1 \qquad \text{Eq. 6}$$

where F_{ij} components are the strength terms and can be evaluated analytically, as shown below, except for F_{12} which is determined through biaxial experiment [32]. However, study have shown that this term has insignificant effect on the final output [33] and setting this to zero would still give adequate accuracy of the results [29].

$$F_1 = \frac{1}{X_T} + \frac{1}{X_C}, \qquad F_2 = \frac{1}{Y_T} + \frac{1}{Y_C}, \qquad F_{11} = -\frac{1}{X_T X_C}, \qquad F_{22} = -\frac{1}{Y_T Y_C}, \qquad F_{66} = \frac{1}{S^2}, \qquad \text{Eq. 7}$$

where

X_T, X_C = axial tensile and compressive strength
Y_T, Y_C = transverse tensile and compressicve strength

S = shear strength

Based from equation 6, the lamina will fail when the polynomial is equal to or greater than 1. Yet, it does not tell the factor of safety (FS) or how much stronger the material is than what is required. The safety factor, which represents the strength of the blade design, can be determined using the Tsai-Wu failure equation. For a given loading, the stress state can be represented as

$$\text{Stress state} = \begin{bmatrix} \sigma_1 \\ \sigma_2 \\ \tau_{12} \end{bmatrix} \quad \text{Eq. 8}$$

With the assumption that when the loading is increased until failure occurs, then the stress at failure is given by

$$\begin{bmatrix} (FS)\sigma_1 \\ (FS)\sigma_2 \\ \tau_{12} \end{bmatrix}$$

Substituting this to equation 6 and rearranging the terms gives equation 10 which is the quadratic equation for the factor of safety.

$$(F_{11}{\sigma_1}^2 + F_{22}{\sigma_2}^2 + F_{66}{\tau_{12}}^2 - F_{11}\sigma_1\sigma_2)FS^2 + (F_1\sigma_1 + F_2\sigma_2)FS = 1 \quad \text{Eq. 9}$$
$$A(FS)^2 + B(FS) + C = 0$$

$$FS = \frac{1}{2A}(-B \pm \sqrt{B^2 - 4AC} \quad \text{Eq. 10}$$

The proposed blade was checked for possible failure. For the base thickness of 5 mm, the failure index for the GFRP blade is 1.202. This implies that there is failure on the blade specifically at the leading edge region near the blade root as can be observed in Figure 15. If the Von mises failure criterion is used, the blade will not fail since the factor of safety based on this criterion would be 7.8, however, closer scrutiny of the ply shows otherwise. Ply by ply analysis of the composite suggested that the failure index decreases from ply 1, which is the outer layer, to ply 5, the inner surface of the blade. Figure 16 shows the failure index through the blade thickness. The results reveal that the failure in GFRP will initiate from layer 1 which is the blade's outer skin. CFRP blade, on the other hand, CFRP has a failure index of 0.422 which indicates that all layers are safe at a blade thickness of 5mm.

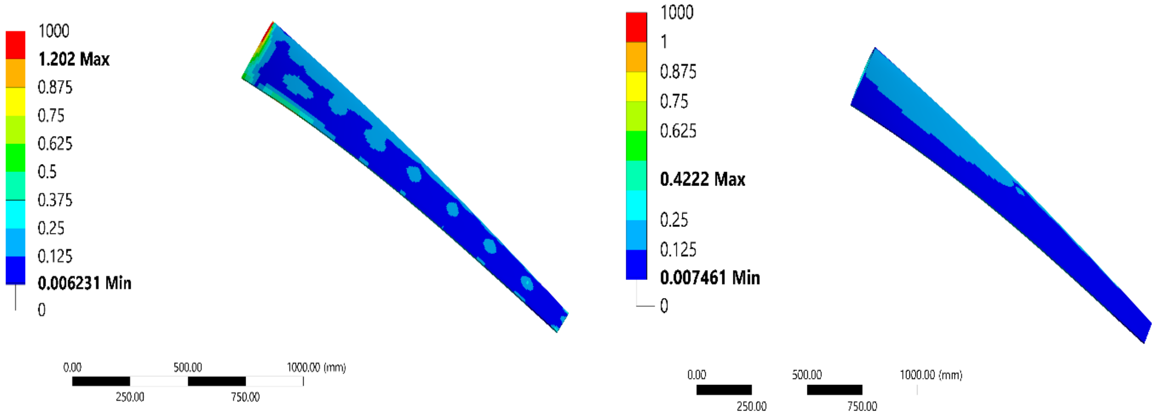

(a) (b)

Figure 15. Tsai-Wu failure factor at 0°ply orientation: a) GFRP, b) CFRP.

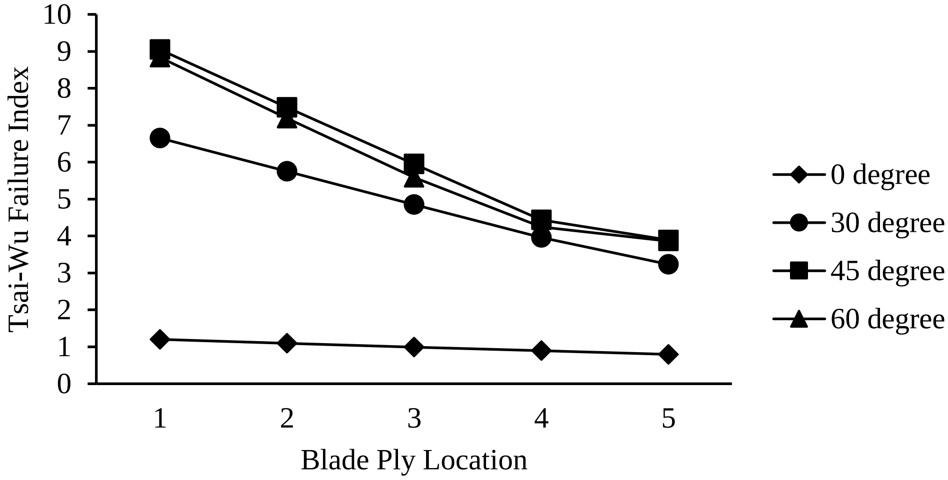

Figure 16. Tsai-Wu failure factor through blade thickness at different ply angle orientations for GFRP.

Since the behavior of composite materials are highly sensitive to the fiber orientation, a parametric study on ply angle and factor of safety was also conducted. Four different fiber orientations shown in Figure 14 were tested and the results showed that the failure index is highest at the fiber angle of 45 degrees. It can also be observed that at ply angles of 30° to 60°, the Tsai-Wu failure indices are all greater than 1. This means that all composite layers located at the leading edge near the blade root in the GFRP blade experienced failure as shown in Figure 18. Although these numbers indicate a failure in the composite layer, physical manifestation may not be evident yet on the blade. Laminate failure may not be catastrophic since it is possible that not all layers fail simultaneously. It is also probable that some plies fail first, as shown in Figure 16, and that the composite can still withstand more loads until all the plies fail [34].

The effects of varying blade thicknesses on the Tsai-Wu reverse failure index were also studied. Figure 17 shows the graph of factors of safety for the two composite materials. It was observed that at a blade thickness of 5 mm, all layers in CFRP are safe with a minimum factor of safety value of 2.369. GFRP material on the other hand, has a factor of safety value below 1. As discussed in the previous section, layers 1 and 2 of GFRP blade experienced failure at the baseline thickness. Four additional thicknesses were also investigated. It can be seen in Figure 17 that as the thickness of the layer increases, the factor of safety of both composites also increases.

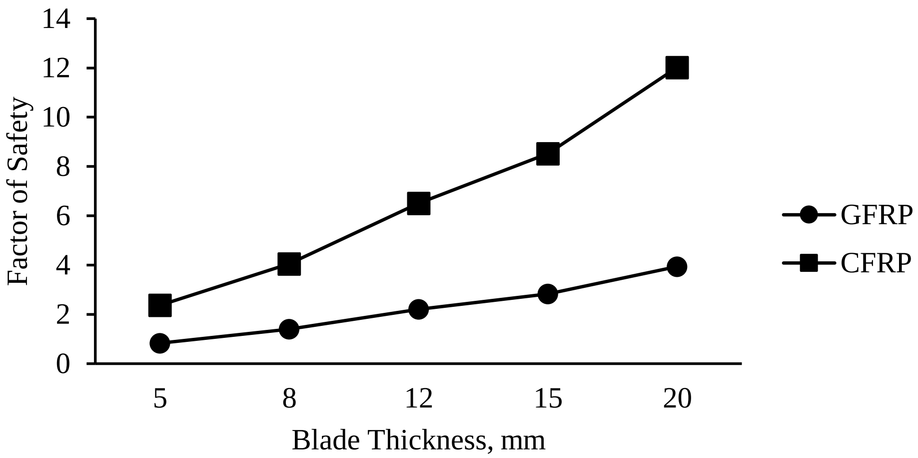

Figure 17. Factors of safety for different blade thicknesses.

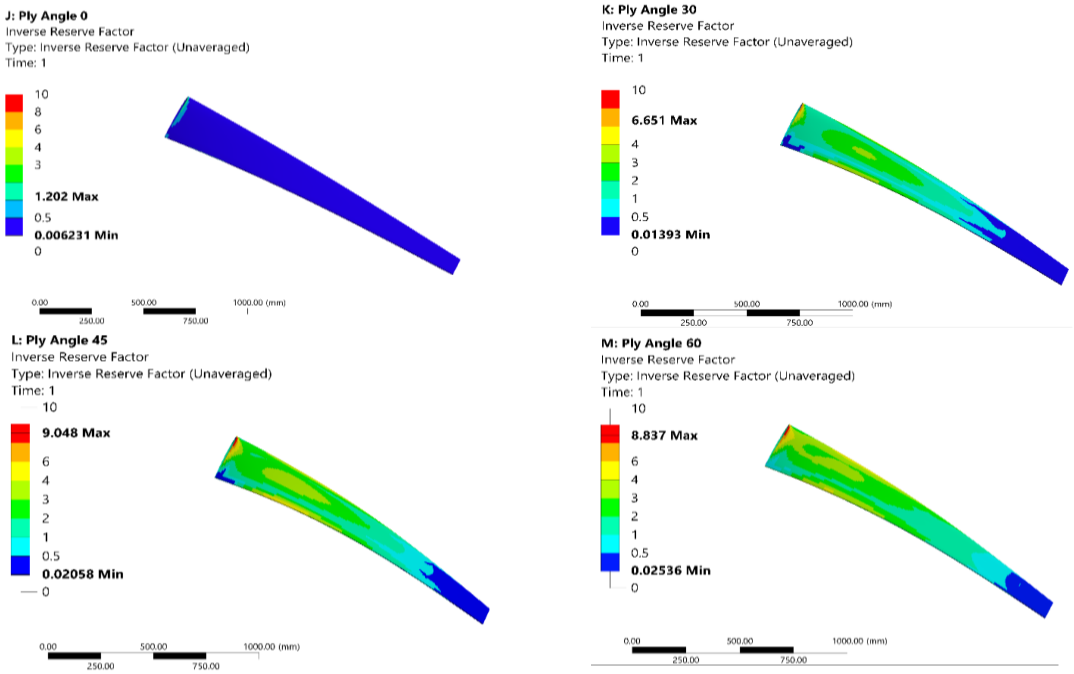

Figure 18. Tsai-Wu failure factor distribution on GFRP blade at baseline thickness and ply orientation.

V. CONCLUSION

A hydrodynamics study coupled with structural response analysis was employed to investigate the integrity of the horizontal axis tidal turbine blade. The optimized blade geometry and force distribution along blade span were determined using Blade Element Momentum Theory (BEMT). These parameters were then used as input information to the structural response study. The structural model using an elliptical tube initially assumed isotropic material properties for verification and validation. Predicted maximum Von Mises stress and maximum nodal displacements are in excellent agreement to analytical solutions. A further study involving the actual blade configuration with a spar was simulated using orthotropic material properties of GFRP and CFRP. A parametric study of ply angle and blade shell thickness was conducted to determine appropriate geometric configurations that will yield the lowest maximum principal stress and blade deformation. It was observed that when the ply angle is increased, the maximum principal stress increases with the worst condition at a ply angle of 45°. This configuration also induces the worst tip deflection. Shell thickness was studied, and results show that increasing the thickness decreased the maximum principal stress owing to a higher cross–sectional resistance. The results of the analysis of the proposed tidal turbine blade also showed that the region a third of the blade span from the blade root is the critical zone. Although the baseline thickness of 5 mm is adequate to meet the applied loading conditions, this might not be enough to withstand extreme and recurring loads. It is highly suggested that a reinforcement material must be added in this critical zone. Nevertheless. all recorded values of stresses fall within the structural strength of the material. Thus, it is determined that the proposed rotor is an improved design given the overall hydrodynamic performance and stress and deformation level analysis results.

REFERENCES

[1] Department of Energy. 2016. Philippine energy plan 2016-2030, J. Chem. Inf. Model. p. 1–101.

[2] Rodriguez FS, 2011. Retrieved from http://123seminarsonly.com/Seminar-Reports/037/59165621-Ocean-Energy.pdf on 2 Dec 2021.

[3] Watchorn M, Trapp T, Sayigh A. 2000. Tidal stream renewable offshore power generation. World Renewable Energy Congress; Oxford Pergamon. VI:2664–7.

[4] Blunden LS, Bahaj AS. 2006. Initial evaluation of tidal stream energy resources at Portland Bill; UK. 31:121–132.

[5] Ordonez-Sanchez S. et al. 2019. Analysis of a horizontal-axis tidal turbine waves using two control strategies.

[6] Abuan B. 2019. A validation study on the performance of a horizontal axis tidal turbine (HATT). Philippine Engineering Journal. 40(1):79–93.

[7] QBlade. Retrieved from http://q-blade.org/ on 20 Apr 2022.

[8] Batten WMJ, Bahaj AS, Molland AF, Chaplin JR. 2007. Experimentally validated numerical method for the hydrodynamic design of horizontal axis tidal turbines. Ocean Eng. 34(7):1013–1020.

[9] Bahaj AS, Batten WMJ, McCann G. 2007. Experimental verifications of numerical predictions for the hydrodynamic performance of horizontal axis marine current turbines. Renewable Energy. 32(15):2479–2490.
[10] Ostowari C, Naik D. 1985. Post-stall wind tunnel data for NACA 44XX series airfoil Sections. [Online]. http://www.osti.gov/energycitations/product.biblio.jsp?osti_id=5791328.
[11] Finnegan W, Allen R, Glennon C. 2021. Manufacture of high-performance tidal turbine blades using advanced composite manufacturing technologies. Appl. Compos. Mater. 28:2061–2086.
[12] Bryden IG, Grinsted T, Melville GT. 2005. Assessing the potential of a simple tidal channel to deliver useful energy, Appl. Ocean Res. 26(5):198–204.
[13] Witten E, Sauer M, Kuhnel M. 2017. Composites market report 2017. AVK (Federation Reinf. Plast. no. September. p. 1–44.
[14] Dayananda HBM, Vijaya P, Padmaraj MK. 2021. Effect of marine environmental conditions on physical and mechanical properties of fiber-reinforced composites – A review. J. Inst. Eng. Ser. C. 102(3):843–849.
[15] Siriruk A, Penumadu D. 2014. Composites: Part B degradation in fatigue behavior of carbon fiber – vinyl ester based composites due to sea environment. Compos. Part B. 61:94–98.
[16] Sen R, 2003. Durability of advanced composites in a marine environment. 19:118–129.
[17] Bazli M, Heitzmann M, Villacorta B. 2022. Durability of fibre-reinforced polymer-wood composite members: An overview. Compos. Struct. 295.
[18] Davies P, Germain G, Gaurier B, Boisseau A, Perreux D. 2013. Evaluation of the durability of composite tidal turbine blades. Philos. Trans. R. Soc. A Math. Phys. Eng. Sci. 371(1985).
[19] Rubino F, Nistico A, Tucci F, Catlone P. 2020. Marine application of fiber reinforced Composites : A review.
[20] Ricker RE, Escalante E, Stoudt M. 2015. Environmental effects on polymer matrix composites.
[21] Lu Z, Xian G, Li H. 2015. Effects of exposure to elevated temperatures and subsequent immersion in water or alkaline solution on the mechanical properties of pultruded BFRP plates, Compos. Part B. 77:421–430.
[22] ANSYS. 2022. Retrieved from https://ansyshelp.ansys.com
[23] Romanenko A, et al. 2012. Composites and their Properties. InTech.
[24] Walczyk D. 2010. An overview of composite wind turbine blade manufacturing. Workshop on Next Generation Wind Power, Rensselaer Polytechnic Institute
[25] ANSYS INC. 2010. Retrieved from http://inside.mines.edu/~apetrell/ENME442/Documents/SOLID187.pdf.
[26] ANSYS. 2022. Retrieved from https://ansyshelp.ansys.com
[27] Norplex-Micarta NorPLYTM 1002 Epoxy Fiberglass Composite, Isotropic. https://www.matweb.com/search/DataSheet
[28] Budynas RG, Nisbett JK, Shigley 2015. Shigley's mechanical engineering design, Mcgraw-Hill Series in Mechanical Engineering. New York: McGraw Hill Education.
[29] Cui WC, Wisnom MR, Jones M. 1992. A comparison of failure criteria to predict delamination of unidirectional glass/epoxy specimens waisted through the thickness. Composites. 23(3):158–166.
[30] Li N, Ju C. 2020. Mode-independent and mode-interactive failure criteria for unidirectional composites based on strain energy density. Polymers (Basel) p. 1–19.
[31] Sun CT, Quinn BJ, Tao J. 1996. Comparative evaluation of failure analysis methods for composite laminates. U.S. Dep. Transp. no. May. p. 133, [Online]. Available: http://trid.trb.org/view.aspx?id=523207.
[32] Tsai SW, Wu EM. 1972. General theory of strength for anisotropic materials. Ohio.

[33] Narayanaswami R, Adelman HM. 1977. Evaluation of the tensor polynomial and Hoffman strength theories for composite materials. J. Compos. Mater. 11(4):366–377.

[34] Kaw AK. 2005. Mechanics of composite materials. 2nd ed. Boca Raton: CRC Press.